3D printed Sr-containing composite scaffolds: effect of structural design and material formulation towards new strategies for bone tissue engineering

Daniele Pierantozzi[1], Annachiara Scalzone[2], Swati Jindal[1], Līga Stīpniece[3], Kristīne Šalma-Ancāne[3], Kenny Dalgarno[2], Piergiorgio Gentile[2], Elena Mancuso[1*]

[1] Nanotechnology and Integrated Bio-Engineering Centre (NIBEC), Ulster University, Shore Road, BT37 0QB, Newtownabbey, United Kingdom
[2] School of Engineering, Newcastle University, Claremont Road, NE1 7RU, Newcastle Upon Tyne, United Kingdom
[3] Rudolfs Cimdins Riga Biomaterials Innovations and Development Centre of RTU, Faculty of Materials Science and Applied Chemistry, Riga Technical University, Riga, Latvia

*Corresponding author: Dr Elena Mancuso, e.mancuso@ulster.ac.uk

Abstract

The use of composite materials, processed as 3D tissue-like scaffolds, has been widely investigated as a promising strategy for bone tissue engineering applications. Also, additive manufacturing technologies such as fused deposition modelling (FDM) have greatly contributed to the manufacture of patient-specific scaffolds with predefined pore structures and intricate geometries. However, conventional FDM techniques require the use of materials exclusively in the form of filaments, which in order to produce composite scaffolds lead to additional costs for the fabrication of precursor filaments as well as multi-step production methods. In this study, we propose the use of an advantageous extrusion-based printing technology, which provides the opportunity to easily co-print biomaterials, starting from their raw forms, and by using a single-step manufacturing and solvent-free process. Poly(e-caprolactone) (PCL), an FDA approved biodegradable material, was used as polymeric matrix while hydroxyapatite (HA) and strontium substituted HA (SrHA), at various contents were introduced as a bioactive reinforcing phase capable of mimicking the mineral phase of natural bone. Three different architectures for each material formulation were designed,

and subsequently the effect of composition variations and structural designs was analysed in terms of physico-chemical, mechanical and biological performance. A correlation between architecture and compressive modulus, regardless the formulation tested, was observed demonstrating how the laydown pattern influences the resulting 3D printed scaffolds' stiffness. Furthermore, *in vitro* cell culture by using TERT Human Mesenchymal Stromal Cells (hTERT-MSCs) revealed that Sr-containing composite scaffolds showed greater levels of mineralisation and osteogenic potential in comparison to bare PCL and pure HA.

Keywords: Polymers, Polymer-matrix composites (PMCs), Functional composites, Extrusion, 3D printing.

1. Introduction

Natural bone is a complex and hierarchically structured composite material based on a specifically mineralized extracellular matrix (ECM) and cells. The ECM consists of 35% organic matrix, mostly collagen, and 65% minerals, mostly of HA crystals, which are found between and within the length of collagen fibers. Moreover, it is possible to find other minerals and microelements, such as carbonates, Sr, Mg etc.[1]. Currently, there is no biomaterial of inorganic or organic nature, which can alone meet the requirements of a scaffold suitable for bone tissue engineering, thus composites are a promising class of engineered biomaterials for bone tissue regeneration. Recently, the combination of synthetic polymers and HA particles and their processing through additive manufacturing technologies have emerged as a promising strategy for the production of 3D bone substitutes [2-4]. Annually, around two million bone graft procedures are performed worldwide in order to repair bone defects stemming from a disease or a traumatic event [5-7]. Bone tissue defects caused by fractures, trauma, disease, and congenital disorders represent an important burden for health care systems worldwide [7, 8]. Over the last twenty years, a wide range of biomaterials,

including bioactive ceramics, metallic biomaterials, biopolymers or biocomposites [6, 9], along with several conventional (*e.g.* foam replication and electrospinning) and most recent additive manufacturing (AM) technologies have been explored to fabricate 3D scaffolds intended for bone tissue repair and regeneration [10-13]. AM techniques offer the promising opportunity to fabricate 3D implants with differences in spatial distribution of porosities and pore sizes starting from a Computer Aided design (CAD) model, and hence enabling the possibility to tailor the device geometry according to the patient needs [14, 15]. Biopolymers currently used for the production of 3D printed (3DP) bone scaffolds include PCL, poly(lactic acid) (PLA) and poly(D,L-lactic-co-glycolic acid) (PLGA) [16-18]. These materials have been widely investigated for their biocompatibility, biodegradation profile and easy processability [19, 20]. Moreover, bioactive ceramics, such as bioactive glasses, β-tricalcium phosphate (β-TCP) [21, 22] and HA [23] have also been widely studied in the Bone Tissue Engineering (BTE) field due to their bioactivity in order to promote osteoinduction as well osteoconduction, and ultimately due to their similarity to the mineral phase of native bone tissue [24]. In addition to this, several research works have proved how the incorporation of trace elements (such as Zn, Mg, Sr) into bioactive ceramic formulations, and therefore their presence into 3D scaffolds, can enhance specific biological responses [25-29]. Particularly, the beneficial effects of Sr substitution into HA are broadly reported [2, 30]. The presence of Sr^{2+} ions has been found to increase osteoid formation and regulates calcium metabolism, stimulates bone formation and enhances collagen synthesis, both *in vitro* and *in vivo* [2, 31, 32]. Also, it promotes osteoblast cell proliferation and enhance Alkaline Phosphatase (ALP) activity [30, 33, 34]. However, 3D printed bone scaffolds made from single biomaterials have some limitations, including but not limited to poor bioactivity, wear resistance and mechanical performance. In essence, they often lack in the ability of matching the anisotropic functional

properties of the different human bone regions [35, 36]. The development of composite structures, based on the combination of polymers and bioactive ceramics, and where the single phase complements each other's strengths and weaknesses, has contributed to solve the shortcomings deriving from the application of a unique biomaterial. However, to create composite scaffolds, the incorporation of a ceramic phase within a polymeric matrix has often involved the use of organic solvents (*i.e.* tetrahydrofuran [3] and chloroform [37]) that carry potential cytotoxic effects to the cells. In order to overcome this hurdle, most of the current strategies rely on the use of FDM 3D printing technologies, where composite scaffolds are produced from filaments [4, 38, 39]. However, in this case raw materials are firstly mixed together, subsequently processed in the form of filaments and ultimately extruded, leading to a multi-step manufacturing process and its inherently additional costs. In this study green chemistry basic principles were followed by using an environmentally-friendly product development strategy, which have been only marginally investigated in the current literature [40-42]. Specifically, a novel solvent-free extrusion-based 3D printing approach, which offers the opportunity to easily co-print biomaterials from their raw forms, has been investigated in this work. Composite scaffolds based on a polymeric matrix of PCL and a bioactive reinforcing phase of HA or SrHA (at various contents: 0 wt%, 10wt% and 20wt%) were produced *via* an advantageous single step and solvent-free extrusion-based 3D printing technology (see Figure 1). Subsequently, we evaluated the effect of scaffolds' structural design and material formulations on mechanical properties and *in vitro* behaviour, in terms of both biomineralisation and osteogenic potential of TERT Human Mesenchymal Stromal Cells (hTERT-MSCs).

2 Materials and methods

2.1 Synthesis and characterization of HA and SrHA powders

HA and SrHA powders were synthesized via aqueous precipitation method [43] according to the protocol as reported in the supplementary file. 2.46 wt% Sr concentration in SrHA powder was targeted based on literature review [44, 45] and our unpublished results. Before composite scaffold manufacturing, the as-synthesized powders were calcined at 650 °C for 2 h. Subsequently, synthesized powders were characterized using the following equipment and methods: X-Ray diffraction (XRD) patterns were recorded using system (X'Pert PRO, PANalytical, Netherlands) operating at 40 KV and 30 mA using a Cu $K\alpha_1$ radiation (λ=1.5406 Å). The XRD patterns were obtained over the range of 2θ from 10° to 70° with an angular step interval of 0.0334°. The X'Pert Data Viewer and X'Pert HighScore software were used for processing and analysing the XRD data. For the phase identification the International Centre for Diffraction Data (ICDD) was used (PDF-2/2005 card #01-072-1243 for HA).

Sr content of the powders was determined using atomic absorption spectrometry (AAS, Varian SpektrAA 880, Australia). Samples were analysed according LVS ISO 11047:1998 standard test method for Sr content determination using electrothermal atomization. Brunauer–Emmett–Teller (BET) method was used to determine the specific surface area (*SSA*) of the powders by N_2 absorption (QUADRASORB SI Kr, Quantachrome, USA). The samples were degassed at room temperature for 24 h prior the analyses. The values of mean sizes of particles were estimated from the N_2 adsorption isotherms using the BET particle diameter (d_{BET}) from the following Eq. 1 by assuming the primary particles to be spherical:

$$d_{BET} = \frac{6}{(q \times SSA)} \quad (1)$$

where *q* is the theoretical density of apatite, which is equal to 3.156 g/cm^3 (according to ISO 13175-3:2012).

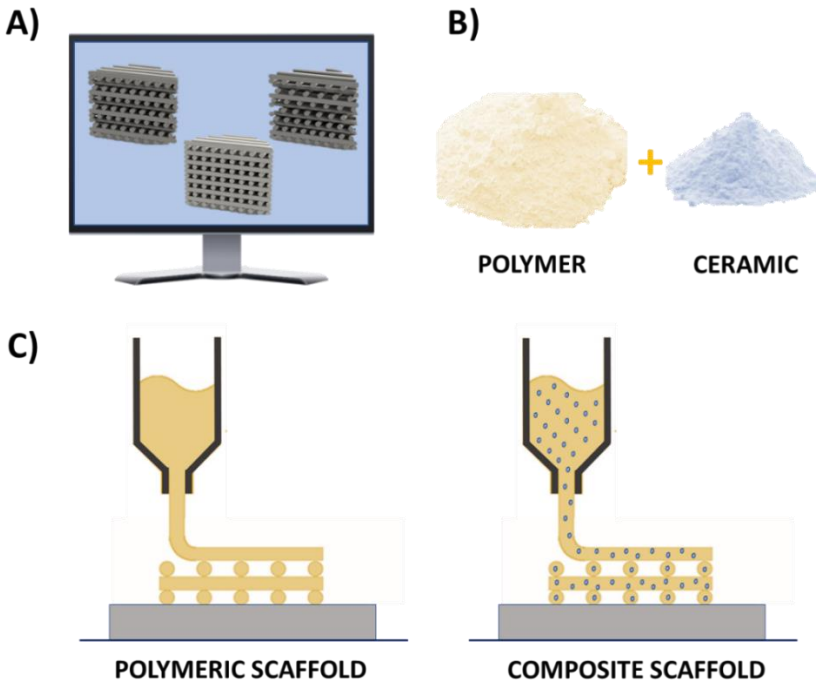

Figure 1: 3D printed scaffold manufacturing route: A) scaffold CAD models, B) precursors' processing and C) extrusion-based scaffold 3D printing.

2.2 Preparation and characterisation of composite material formulations

Powdered PCL with a relative molecular weight of 50 kDa and a particle size <600 µm (Polyscience Europe, Germany) and HA, SrHA calcined powders were used for this study. Firstly, raw powder materials were mechanically mixed together at room temperature. In order to avoid the clogging of the needle during the extrusion process and prior to mix with the PCL, both HA and SrHA powders were ground and then sieved using an analytical sieve with a mesh size of 106 µm. Afterwards, PCL, HA, and SrHA powders were mechanically mixed together in different proportions, as reported in Table 1. The so obtained composite powder mixtures were labelled as PCL/10HA, PCL/10SrHA, PCL/20HA and PCL/20SrHA, while pure PCL was used as control. In

order to ensure a homogenous mixing of the powders, the resulting powder mixtures were kept overnight on a mechanical roller (Stuart Scientific, UK). Prior to start the printing process, the ready to be used composite powders were stored in a desiccator until usage. The PCL as well as the composite powders were analysed with Attenuated Total Reflectance Fourier Transform Infrared Spectroscopy (ATR-FTIR). The analyses were carried out with a Nicolet iS5 by Thermo Scientific, equipped with an iD5 ATR diamond crystal window. All the spectra were measured in the spectral range between 500 cm^{-1} and 4000 cm^{-1} and a resolution of 4 cm^{-1}. In addition to this, the morphology of the precursor materials was investigated *via* Scanning Electron Microscopy (SEM, Hitachi FE-SEM SU5000) at voltage of 2 kV and working distance of 5.6 mm. Before imaging, the samples were firstly gold coated and subsequently fixed on aluminium stubs by using carbon tape. The images were collected through the equipment's software.

Table 1:Code and composition of the precursor material formulations.

CODE	COMPOSITION (wt%)
PCL	100% PCL
PCL/10HA	90% PCL + 10% HA
PCL/10SrHA	90% PCL + 10% SrHA
PCL/20HA	80% PCL + 20% HA
PCL/20SrHA	80% PCL + 20% SrHA

2.3 Design and manufacturing of 3D composite scaffolds

As widely reported in the literature, one of the most critical characteristics of a 3D bone substitute is the capacity to structurally fit to the host tissue defect and mimic its inherent biomechanical properties [5, 7]. In this study composite scaffolds were developed according to three different internal architectures. A representation of the inner geometry, external shape and the cross-section of the three architectures is reported in Figure 2. Architecture 1 has been chosen because it represents the most widely applied tissue-like structure, and it can be considered as a control pattern

[3, 14, 46]. This was produced using a laydown pattern of 0/90° to create porous structures (e.g. the layer 3 is orthogonal to layer 2 and is printed in the same relative position of layer 1). The distance between the strands was set at 0.8 mm, calculated from the centre of the strands. This architecture will be named hereafter as Not Shifted Not Graded (NSNG). Architecture 2 has been selected after the review of the current literature, where is clearly demonstrated that the offset pattern allows an increased pore interconnectivity and a better in vitro behaviour [17, 47, 48]. The shifted pattern was realised using the same 0/90° pattern with 0.8 mm distance between strands, although in this case the layers with the same orientation were produced with an offset distance equal to half the distance between strands (0.4mm). This will be called Shifted Not Graded (SNG) architecture. Architecture 3 has been developed in order to produce a structure that could mimic the gradient architecture of human bone tissue [49-51]. This pattern was obtained maintaining the previous described shifted pattern, and adding a porosity gradient moving from the bottom to the top of the 3D structure. The porosity gradient structure was achieved by increasing the distance between the strands progressively. Specifically, for the first four layers the distance between the strands was set to 0.8 mm; subsequently, the distance was increased by 0.1 mm every two layers. This architecture will be named hereafter as Shifted Graded (SG) structure. To create computer models for printing, cylindrical geometries with 7 mm diameter and 6 mm height were designed in Solid Edge™ 3D software. These were then sliced by using BioplotterRP 3.0 Software (EnvisionTEC, Gladbeck, Germany), in order to obtain 14 layers overall (420 µm slicing thickness). The extrusion-based printing process for the fabrication of the composite scaffolds was carried out as described in a previous study [52], by using a 3D-Bioplotter system (EnvisionTEC, Gladbeck; Germany). Briefly, about 4g of material in form of powder was weighted and introduced into a stainless-steel cartridge. Subsequently, the cartridge was placed into the high-temperature

printing head and heated up so that the material was allowed to melt. A nozzle with 0.4mm internal diameter was used to extrude all the material formulations. Following on an initial optimisation process, final printing conditions (temperature, pressure, speed, pre- and post-flow) were set for each composition by using the operating software VisualMachine 2.8.115 (EnvisionTEC, Gladbeck; Germany), and as reported in Table 2.

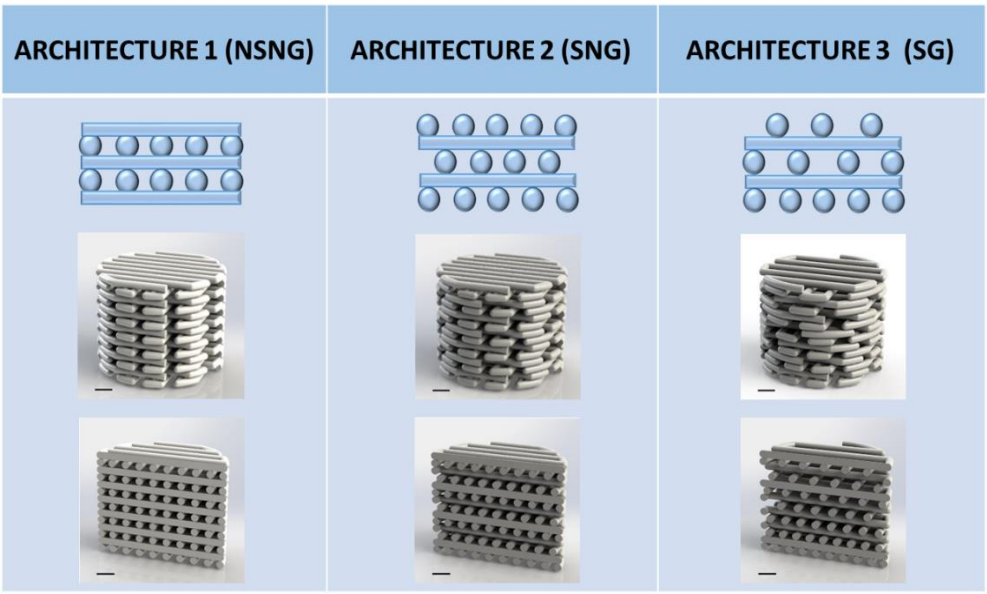

Figure 2: 3D scaffold architectures (1= NSNG, 2= SNG and 3= SG) and corresponding CAD model rendering of the 3D volume and cross section.

Table 2: Optimised printing parameters.

	PCL	PCL/10HA	PCL/10SrHA	PCL/20HA	PCL/20SrHA
Temperature (°C)	130	130	130	140	140
Pressure (bar)	6.00	6.20	6.20	6.40	6.40
Speed (mm/s)	0.60	0.50	0.60	0.50	0.60
Pre-flow (s)	0.45	0.80	0.75	0.75	1.00
Post-flow (s)	0.10	0.10	0.10	0.10	0.10

2.4 Physico-chemical and mechanical characterisation of 3D bioplotted scaffolds

Thermogravimetric analysis (TGA) was performed in order to examine both the printed materials' thermal behaviour and to assess the actual ceramic content in the polymeric matrix. The equipment

used for the test was a TGA2 METTLER TOLEDO™ with a resolution of 1 µg, weighing accuracy of 0.005% and weighing precision of 0.0025%. The dedicated software STARe™ was used as an interface with the device to process the obtained information. TGA analysis was performed in air and the initial weight of the samples was measured approximately around 10 mg for every test. The resulting curves were normalized to the initial mass weight for each sample. Three samples for each composition were tested in a range of temperature between 25 and 800 °C with a heating rate of 10 °C/min. Microcomputed tomography (Micro CT) analysis was performed to evaluate the architecture and topology of the printed scaffolds. A Bruker Skyscan 1275 (Bruker, Kontich, Belgium), with a Hamamatsu L11871 source and 3 MP active pixel CMOS flat panel detector was used. The scans were conducted under 40 kV and 230 µA for an exposure time of 49ms and a pixel resolution of 10 µm. Scans were reconstructed, resliced and analysed using NRecon, CTvol and CTAn software (Bruker, Kontich, Belgium).

Then, in order to investigate 3D printed scaffolds' surface morphology and to verify strands' dimension, SEM analysis was performed using the same equipment reported in the paragraph of section 2.2; a voltage of 5 kV and a working distance of 5 mm were used for all the investigated samples, which were firstly gold coated and subsequently fixed on aluminium stubs.

Scaffold porosity (P) was first calculated theoretically through the formula reported in Eq. 2 [53]:

$$P = 1 - \frac{\pi d_1^2}{4 d_2 d_3}\ x\ 100 \qquad (2)$$

using the assigned printing parameters as elements for the calculation, and where d_1 is the plotted strand diameter, d_2 is the distance between strands and d_3 is the thickness of the layer (see Figure S1). In addition, the overall porosity was calculated experimentally through the actual dimensions of d_1, d_2 and d_3 measured from the 2D sections obtained from the MicroCT analysis. The

measurements on the 2D images were carried out using ImageJ, and three different samples were analysed for each formulation as well as architecture investigated.

Compression tests were performed using an Instron 5500S testing machine, equipped with a 500N load cell. Specimens with a 7 mm diameter and 6 mm height were compressed in the longitudinal direction at a constant crosshead speed of 0.5 mm/min up to a deformation of 70% or until the safety range of the load cell was reached. The specimens were subjected at 2N preload before the starting of the test. Five specimens were tested for each type of 3D printed scaffold. The Young's Modulus was obtained from the slope of the linear region of the stress-strain response curve on the early stage of compressive loading.

2.5 *In vitro* biological evaluation

2.5.1 *Cell culture and seeding protocol*

Human TERT immortalised bone marrow stromal cell line was kindly supplied by Prof P. Genever (York University) at passage 84. Briefly, cells were grown at 37°C, 5% CO_2, in Dulbecco's Modified Eagle Medium (DMEM; Sigma, UK) supplemented with 10% foetal bovine serum (FBS; Thermo Fisher, UK) and a 1% Penicilin Streptomycin (P/S; Sigma, UK). After the expansion, cells were used between passage 86 and 90. Prior to cell seeding, the PCL, PCL/20HA and PCL/20SrHA scaffolds with a 7 mm diameter and 2.5 mm height were sterilized with 70% ethyl alcohol solution (ETOH; Sigma, UK) for 20 minutes and treated with Sudan Black (SB) to limit auto fluorescence. Each scaffold was covered with 50 µL of SB solution (0.3% w/v in Ethanol), incubated for 20 minutes at 37 °C and washed properly twice with Dulbecco's phosphate-buffered saline (PBS; Sigma, UK). Then samples were sterilized under a UV lamp for 30 minutes and placed in 48-well plate. hTERT MSCs were suspended in DMEM and seeded on each sample at a concentration of

$1.5x10^5$ cells per scaffold and incubated at 37 °C, 5% CO_2 for 30 min. Then, fresh DMEM was added up to 500 µL of volume.

2.5.2 Cell viability, morphology and proliferation tests

The cytocompatibility of the samples was assessed with the Live/Dead assay (LIVE/DEAD® Cell Imaging Kit; Life Technologies, UK), according to the manufacturer's instructions. This fluorescence-based kit combines calcein AM and ethidium bromide to yield two-colour discrimination of the population of live (green) from the dead (red) cells. In brief, 4µM ethidium homodimer-1 and 10µM calcein were dilute in PBS. Each sample was washed twice with PBS before incubation with the staining solution for 30min at 37°C. Images were collected at day 1 and day 3 using a Nikon A1R inverted confocal microscope. The immunostaining analysis were performed fixing in pre-warmed 4% w/v paraformaldehyde (PFA) the samples for 15 minutes and cells were consequently permeabilised using 0.1% v/v Tween20® (Sigma, UK) in PBS for three washes. The cells cytoskeleton was stained using Phalloidin, prepared using phalloidin-tetramethylrhodamine B isothiocyanate (1:1000 in 0.1% PBS/Tween20®) for 20min at room temperature. Then, for staining the cells nuclei samples were washed with 0.1% PBS/Tween20® solution and immersed in DAPI solution (Vector Laboratories, UK) (1:2500 in 0.1% PBS/Tween20®) for 20 min at RT. At day 7 images were collected using a Nikon A1R inverted confocal microscope. Cells metabolic activity was analysed with the MTT (Thiazolyl Blue Tetrazolium Bromide) assay using a standard kit provided by Sigma, UK. The MTT solution was prepared following the supplier instructions, obtaining a final concentration of 5mg/mL, in PBS and the stock solution was mixed with serum-free DMEM without phenol red. Samples were incubated for 4 hours at room temperature protected from light. Then, MTT media was removed and replaced by 400 µL of dimethyl sulfoxide (DMSO, Sigma, UK) for each well and the plates

agitated for 30 minutes on a Stuart Mini Microtitre Plate Shaker, in order to dissolve the formazan crystals, a product of digestion of the MTT by the cell. Then, 200µl of each well solution (in duplicate) was transferred to a clear bottom 96-well plate and a Filter-based multi-mode microplate reader (Biotek, UK) was used to measure the absorbance at 570 nm. Measurements were taken in triplicate after 1, 3, 7, 14 and 21 days. The estimation of the cell number was performed based on a standard curve, generated by seeding hTERT-MSCs at different densities (0, 5 000, 10 000, 30 000, 50 000, 100 000 and from there on up to 500 000 with a 50 000 increase).

2.5.3 Cell osteogenic differentiation

Alkaline Phosphatase (ALP) activity as an early osteogenic differentiation marker was measured by using the ALP assay kit (Sigma, UK) up to 21 days. Samples were washed with PBS after removing the media and fixed in 4% PFA. Following this, cells were washed in 0.1% PBS/Tween20® solution and alkalinised with water/0.1M Tris solution (Sigma, UK). Then, the alkaline solution was replaced by 1ml of ALP solution, and samples were incubated at room temperature for 30 minutes protected from light. 100µL of solution was then taken from each well and placed in a clear-bottom 96-well plate to quantify the ALP activity. The reading was performed with a spectrometer (ELx800; BioTek Instruments, UK) at 405nm. The results are showed based on the values obtained from a standard curve, created by placing different concentrations of 0.1M Tris/ALP into a 96-well plate.

2.5.4 Calcium detection: Alizarin Red Staining

Samples were fixed in 4% PFA and washed in PBS twice and stained with 1mL of Alizarin Red solution (Sigma) for the detection of Calcium. The incubation was performed at room temperature for 15 minutes. Then, samples were washed with deionised water multiple times and dried overnight at 60°C in a 5% CO_2 atmosphere. Imaging of the samples was performed on a

stereomicroscope equipped with a digital colour camera (Leica Microsystems). The experiment was performed at day 0, 14 and 21.

2.6 Statistical analysis

Tests were performed at least in triplicate for each sample. The results were represented as mean ± standard deviation. Differences between groups were determined using One-way analysis of variance (ANOVA) with Turkey's multiple comparison test using levels of statistical significance reported in each figure's caption.

3 Results and Discussion

3.1 Composite powders preparation and characterisation

Several studies on Sr-containing biomaterials in various forms indicate that even as small amounts as 0.1% of Sr might be enough to have an impact on both bone formation and remodelling [30, 33]. In this work HA powders containing 2.46 wt% (24.6 mg Sr per g of the powder) of Sr was used as filler for composite scaffolds. The quantitative amount of Sr in the samples determined by AAS is shown in Table 3. For SrHA sample the measurements confirmed presence of Sr in the powder. Even though the measured concentration was similar to what was expected, i.e. nominal concentrations, the total uptake of ions in the powders was affected due to the used synthesis technique, most likely, during the washing steps, which aimed to remove impurities and reaction residues.

Table 3: Chemical composition of calcined (650 °C, 2 h) HA and SrHA powders.

Sample designation	Chemical formula	Nominal Sr concentration (wt%)	Measured Sr concentration (wt%)
HA	$Ca_{10}(PO_4)_6(OH)_2$	-	-
SrHA	$Ca_{9.52}Sr_{0.48}(PO_4)_6(OH)_2$	2.46	3.10 ± 0.30

XRD patterns (see Figure 3) of the calcined HA and SrHA powders used for preparation of the composite scaffolds were compared with that of standard HA powder by ICDD PDF-2/2005 card #01-072-1243. For all powders a good agreement between the experimental data and the standard hexagonal HA structure was obtained. Hexagonal structure of the powders was confirmed by the triplet between 30.5 deg and 33.5 deg with a pronounced peak at 31.78 deg (211 plane) overlapping with two others at 32.13 deg (112 plane) and 32.91 deg (300 plane). Broad and overlapping characteristic XRD peaks indicated that the powders consist of nanostructured HA particles with a high surface area [54]. No extraneous phases were detected in the examined 2θ range. Thus, the detected amounts of Sr were assumed to refer to the ones incorporated in the HA structure. The nanocrystalline nature showed by XRD analysis was confirmed by the BET data summarized in Table S2. However, BET analysis showed no significant differences between SSA values between the powders. Thus, it can be concluded that the incorporation of Sr in the HA structure in this case has a negligible effect on the particle size and morphology, which is also shown in the SEM micrographs (Figure S2).

ATR-FTIR analysis was conducted in order to assess the presence of functional groups within the precursor powders (see Figure 4), prepared as previously described. PCL spectra showed the characteristic bands of this polymer in agreement with the literature [55, 56], corresponding to the typical CH_2 symmetric and asymmetric bands respectively at 2940 cm^{-1} and 2860 cm^{-1}, the carbonyl stretch at 1720 cm^{-1}, the C=O group peak at 1723 cm^{-1}, the backbone C─O and C─C stretching in the crystalline phase 1293 cm^{-1}, as well as the C─O─C band, 1164 cm^{-1}. In relation to HA powders (see Figure 4(A)), absorbance bands corresponding to the characteristic HA PO_4^{3-} groups appear at 560 cm^{-1} and 600 cm^{-1} (O-P-O bending mode v_4), 961 cm^{-1} (P-O stretching vibration mode v_1), and 1022 cm^{-1} and 1088 cm^{-1} (P-O stretching vibration mode v_3) cm^{-1}. The

band at 631 cm^{-1} can be assigned to bending vibrations of the structural OH group. The O-H stretching of OH groups is observed at 3571 cm^{-1} [57]. As reported in Figure 4(B), no significant differences were observed in the SrHA spectra in comparison to the one referring to the pure HA (Figure 4(A)) [43]. Regarding the mechanically mixed composite powders, the ATR-FTIR results (Figure 4(A, B)) showed that PCL and ceramic phases were both present. Specifically, all the as prepared composite powders (PCL/10HA, PCL/20HA, PCL/10SrHA and PCL/20SrHA) showed the C=O group peak at 1723 cm^{-1}, the PO_4^{3-} group at 560/600 cm^{-1} and 961/1022/1088 cm^{-1} along with the CH_2 symmetric and asymmetric bands.

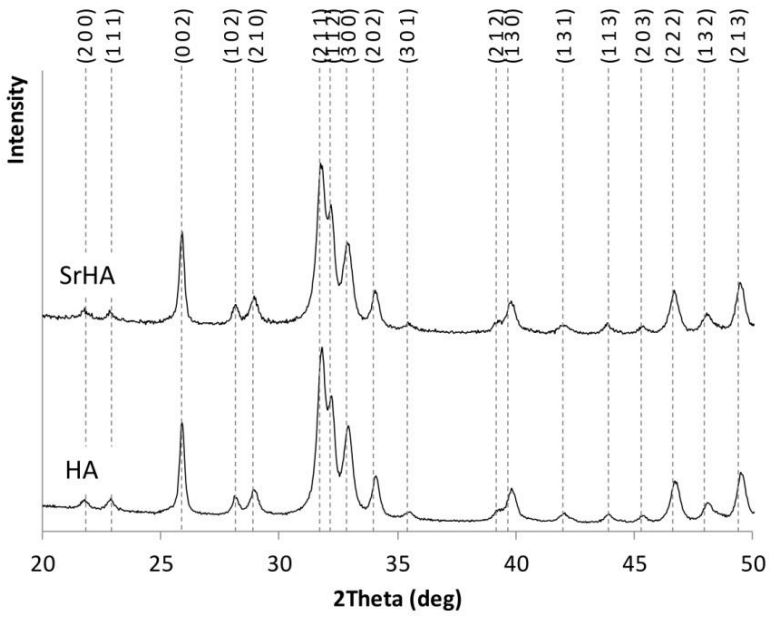

Figure 3: XRD patterns of calcined (650 ºC, 2 h) HA and SrHA powders

3.2 Composite scaffolds: manufacturing, physico-chemical and mechanical characterisation

3D scaffolds were printed according to the conditions listed in Table 2, after an initial optimisation process of the following parameters: printing temperature, pressure, speed, pre-flow and post-flow. No substantial differences were recorded in terms of printing parameters between PCL/10HA and

PCL/10SrHA, which might be dictated to the similar precursors' morphology, and in comparison to the pure PCL scaffolds; whereas increasing the content of HA phase above 10 wt% required higher printing temperature as well as pressure for the processing of mechanically mixed composite powders. Also, the content of the inorganic component in the extruded materials was analysed by TGA, and the results are reported in Figure S3 as average of three samples. As shown, at the temperature of 600 °C, there is no residual substance for pure PCL, indicating this material was completely thermal-decomposed at that temperature. Regarding the composite formulations, the residue of inorganic material for PCL/10HA, PCL/10SrHA, PCL/20HA and PCL/20SrHA were 10.12 ± 0.9 wt%, 11.55 ± 1.2 wt% 20.80 ± 2.5 wt% and 17.90 ± 2.9 wt% respectively, which are consistent with the wt% of inorganic component of the as prepared blends. Also, similarly to the recent findings reported by Huang et al. [58], it was observed that the addition of the nano-ceramic particles slightly reduced the degradation temperature of the printed composite scaffolds. However, since the printing temperature used in our study was below 150 °C, it can be concluded that the manufacturing process did not cause any material loss.

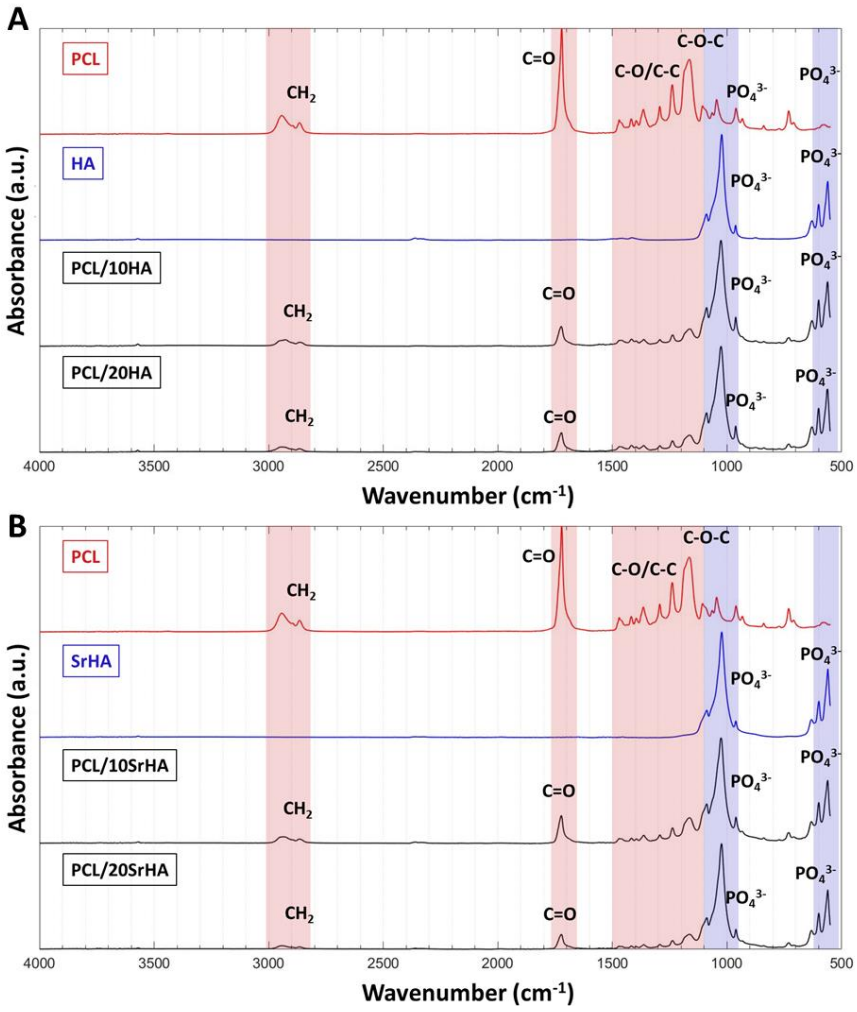

Figure 4: FTIR spectra of A) PCL, HA and composite HA-based powders and B) PCL, SrHA and composite SrHA-based powders.

Next, the topology as well as the architecture of the 3D printed composite scaffolds were investigated through a non-destructive technique. In Figure 5 microCT reconstructions for all the printed samples are reported. MicroCT investigations indicated the actual presence of the ceramic particles homogenously distributed within the PCL matrix, both on the surface and in the inner part, as it is possible to visualise from the 3D reconstructions of the cross sections. In addition, the morphology of the 3D printed samples was observed by SEM. As shown in Figure S4, all the scaffolds possessed well-defined strands' structure. Moreover, the pure PCL scaffold as well as the

composites with the lower ceramic content revealed a smooth surface (Figure S4 (B, D, F)) while the PCL/20HA and PCL/20SrHA (Figure S4 (H, J)) presented a large number of white spots. According to both microCT reconstructions as well as SEM micrographs, all the printed scaffolds displayed a high level of fidelity to the original CAD model, further proving the potential of extrusion printing process for the production of custom made devices, as extensively demonstrated in recent years [13, 38, 40]. The measured total porosity values for the fabricated composite scaffolds are reported in Table 4. According to the data, it is worth noting that theoretical porosity values calculated through the formula reported in Eq.1 are consistent with the experimental data derived from microCT scans, thus demonstrating the reliability of the approach used. Furthermore, from the analysis of the data displayed in the table, for all the investigated composite scaffolds the total porosity values were found to be in the range of human trabecular bone porosity (30% - 90%) [59], with the NSNG and SNG architectures showing similar results (~ 40%).

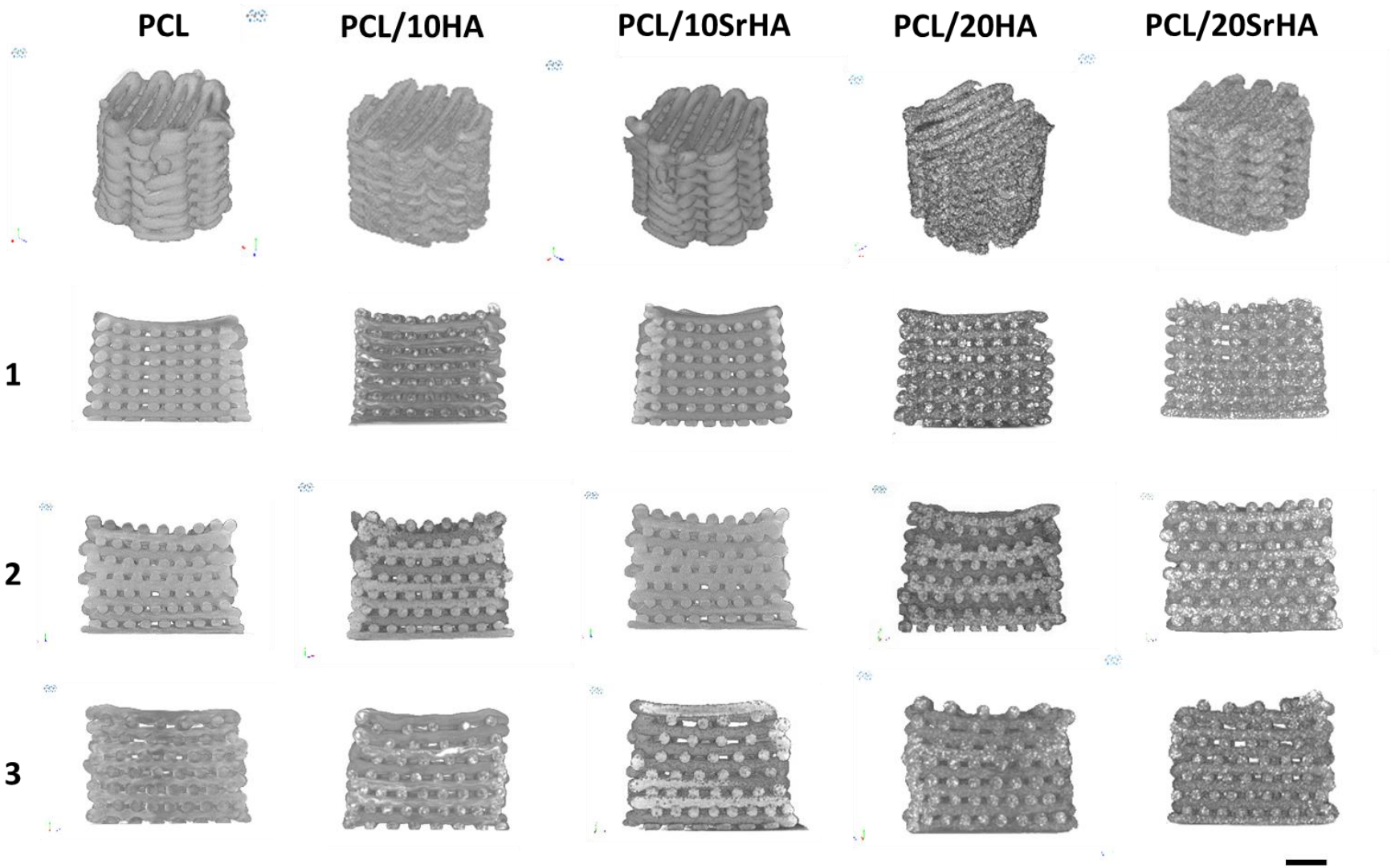

Figure 5: Representative microCT images of all the 3D printed scaffolds and cross section of the three different architectures produced (1= NSNG, 2=SNG and 3= SG architecture); [scale bar = 2mm].

Table 4: Theoretical and experimental total porosity values of 3D printed scaffolds

Code	Total porosity (%)	
	Theoretical	Experimental
PCL – NSNG	41.56	36.6 ± 1.4
PCL – SNG		36.6 ± 1.5
PCL – SG	52.43	50.4 ± 0.8
PCL/10HA – NSNG	41.56	40.1 ± 1.5
PCL/10HA – SNG		42.2 ± 1.1
PCL/10HA – SG	52.43	54.4 ± 1.8
PCL/10SrHA – NSNG	41.56	42.3 ± 1.8
PCL/10 SrHA – SNG		43.0 ± 2.5
PCL/10SrHA – SG	52.43	52.9 ± 1.6
PCL/20HA – NSNG	41.56	42.4 ± 0.7
PCL/20HA – SNG		39.4 ± 1.5
PCL/20HA – SG	52.43	48.7 ± 1.6
PCL/20SrHA – NSNG	41.56	37.7 ± 1.5
PCL/20SrHA – SNG		36.6 ± 1.1
PCL/20SrHA – SG	52.43	47.5 ± 1.2

The compressive mechanical properties of pure PCL and composite scaffolds based on PCL/HA and PCL/SrHA fabricated by extrusion 3D-printing were investigated as function of the different architectures. Overall the produced composite scaffolds exhibited mechanical properties in a range of values consistent with recent research studies, in which melt extrusion 3D printing systems were used [42, 46, 60]. Moreover, the mechanical performances of all the specimens were found to be about one order of magnitude higher with respect to 3D printed composite scaffolds manufactured through a solvent-based extrusion system [61]. Representative compressive stress–strain curves for the NSNG, SNG and SG 3D printed scaffolds are shown in Figure 6 (A, B, C), these results are consistent with the findings reported by Jiang et al. on the compressive properties of PCL/HA scaffolds produced with a similar manufacturing process [60]. Furthermore, as expected we observed a correlation between architecture, porosity and compressive modulus (Figure 6(D)).

Regardless of the formulation tested, NSNG and SNG architectures are stiffer in comparison to the more porous SG architecture (mean porosity ~ 50%), indicating how the laydown pattern influences the porosity values of the scaffold, which in turn result to affect its mechanical behaviour. From Figure 2 it can be seen that the SG architecture is achieved through reducing the amount of material in the upper layers. This enhances clearly makes the scaffold overall more porous, and means that these layers are more compliant when compressed. However, no significant differences were recorded between the NSNG and SNG architecture. Moreover, it was possible to conclude that the mechanical behaviour in compression is broadly unaffected by the formulation, and to some extent it can be tuned through the adjustment of the laydown pattern within the scaffold. Furthermore, the inclusion up to 20 wt% of HA or SrHA calcined powder in the polymeric matrix led to small and not statistically significant differences in the values of Young's moduli in comparison to bare PCL scaffolds. In accordance to Myoung Hwan Kim et al. [46] and Gómez-Lizárraga et al. [62], this behaviour may be recognised as a consequence of the mixing process of the two composite phases, which was performed through physical rather than chemical blending. Therefore, in light of these results, and based on the findings reported by Yilgor et al., according to which a shifted not graded design can lead to a better *in vitro* response [47], the PCL/20HA and PCL/20SrHA formulations printed with a SNG architecture were selected for further analysis, whereas bare PCL was used as control.

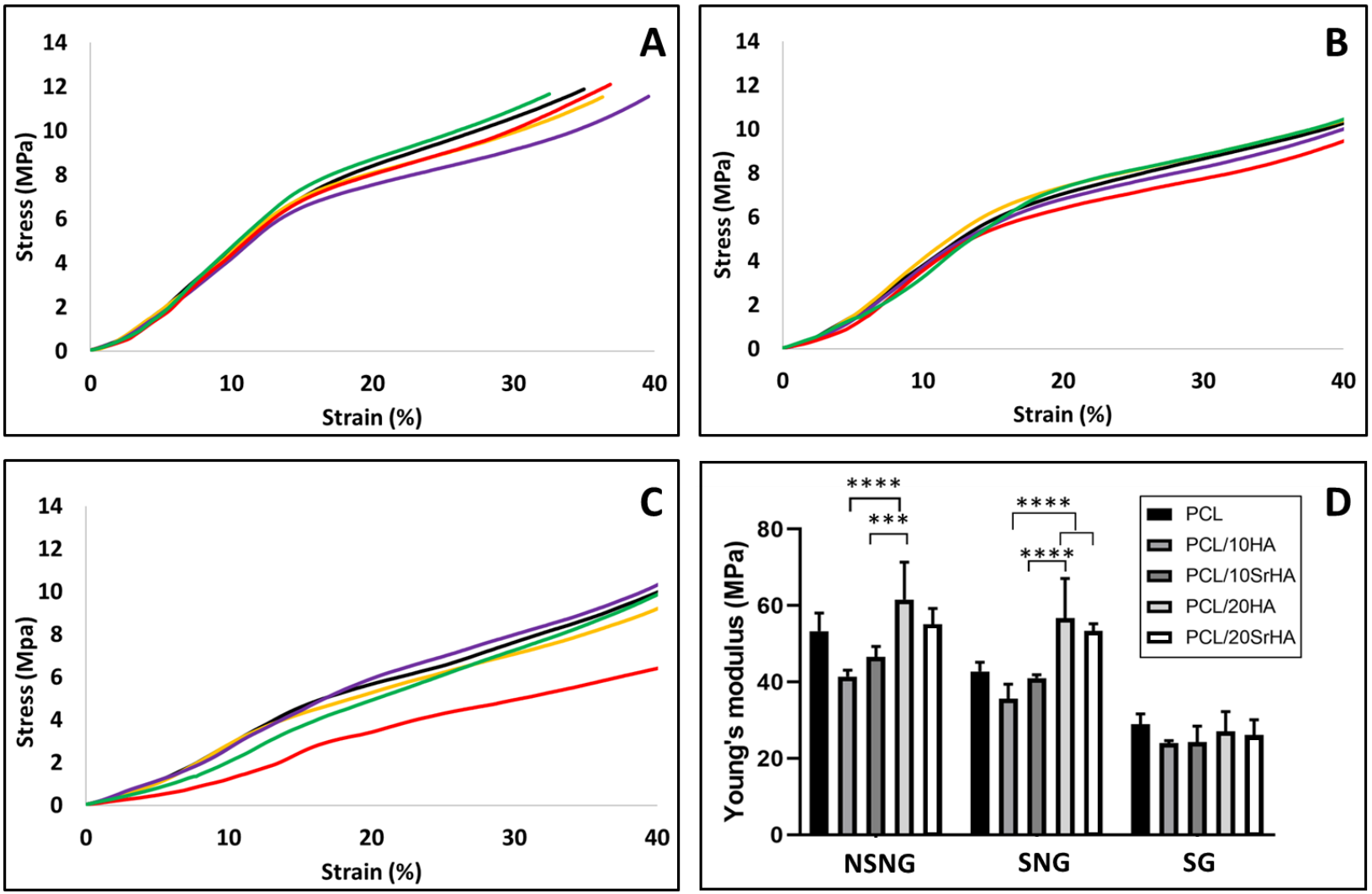

Figure 6: Compressive stress-strain curves for: A) NSNG, B) SNG and C) SG architecture (— PCL, — PCL/10HA, — PCL/10SrHA, — PCL/20HA, — PCL/20SrHA) and D) Young's Modules values of 3D printed scaffolds. Statistics: p<0.0001 (****), p=0.0005 (***).

3.3 Biological *in vitro* scaffold performance

3.3.1 Cells viability, immunostaining and proliferation

In order to evaluate the cytocompatibility of the 3D printed scaffolds, cells were seeded on the top of the scaffolds and cultured. All the scaffolds showed a favourable support for cells attachment, growth and proliferation. Live/Dead staining showed round-shaped live cells (green) attached to the scaffold in all the three samples at 24h while the presence of HA phase in the PCL/20HA and PCL/20SrHA samples demonstrated to promote cells spreading, communication and agglomeration compared to the PCL scaffolds (Figure 7a). In all the cases few dead cells (red) were observed. This was further confirmed by immunostaining (nuclei stained with DAPI and the cytoskeleton with rhodamine-phalloidin) that confirmed the scaffolds compatibility and the tendency of the hTERT MSCs to form agglomerates mainly in the samples where was present the HA phase compared with the bare PCL samples, characterised by a more homogenous distribution of the cells within all the scaffold (Figure 7a).

The proliferation of hTERT MSCs was qualitatively detected by MTT assay (Figure 7b). In fact, as shown in Figure 7b it was registered a positive trend on cell proliferation at day 3 and day 7 with a highly significant increase in the number of cells for all samples at day 21 compared with all the previous time points ($p<0.0001$) (Figure 7b) without significant differences among the three groups, meaning that the all the 3D printed structures allowed cellular proliferation.

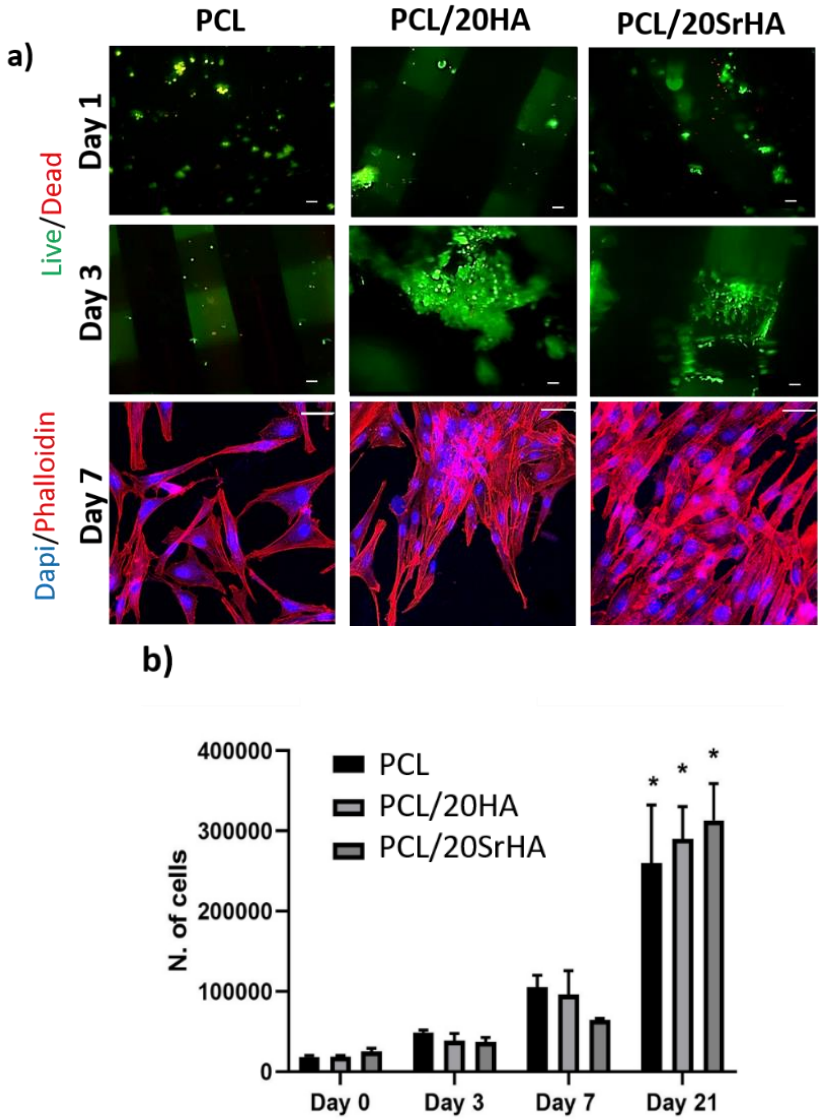

Figure 7: a) Cytocompatibility evaluation of the 3D printed PCL, PCL/20HA and PCL/20SrHA Sr scaffolds: Live/Dead images of cells seeded after 1 day and 3 days of culture (live cells in green and dead cells in red) (top images) [Bar=100µm]; Immunostaining images of cells seeded after 7 days of culture (nuclei in blue and cytoskeleton in red) (bottom images) [Bar=20µm]. b) Estimation of cell number using MTT absorbance values and a calibration standard curve up to 21 days. Statistics: p<0.0001 (*).

3.3.2 Osteogenic potential and mineralisation

ALP is an early marker of osteogenic differentiation and higher ALP activity reveals strong cell-cell and cell-matrix interactions [30]. From the graph in Figure 8a, at day 0 the ALP value is

significantly higher in the samples without Sr ($p<0.0001$), while at 14 days of culture Sr containing scaffolds show a delay in the osteogenesis as confirmed by the Alizarin red assay (Figure 7b) with a lower formation of calcium deposits compared with HA containing scaffolds [2]. Furthermore, an obvious decrease in the ALP activity was observed after 21 days of culture in all samples and this is related to cells mineralisation [63] as demonstrated by the visual presence of minerals stained with Alizarin Red (Figure 8b). In fact, all the samples showed a more relevant presence of calcium deposits at 21 days compared with the previous time points (except for few deposits visible on the PCL/20HA samples after 14 days). Particularly, after 21 days of culture the presence of Sr seemed to enhance the mineralisation phenomenon, as demonstrated by the highest presence of red stained-deposits in this samples compared to the other samples (Figure 8b).

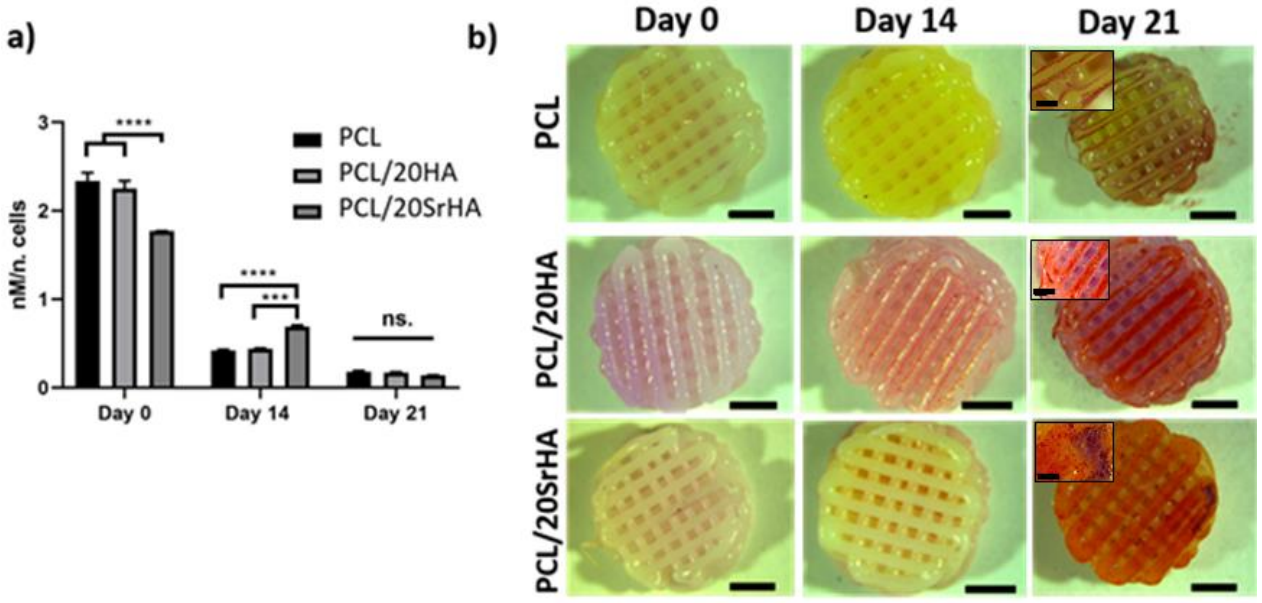

Figure 8: a) Osteogenic differentiation of hTERT MSCs seeded on the PCL, PCL/20HA and PCL/20SrHA scaffolds through measurement of ALP activity up to 21 days. Statistics: $p<0.0001$ (****) and $p< 0.001$ (***). b) Alizarin red staining of cell-seeded scaffolds: images collected at day 0, 14 and 21 [Bar = 2mm]. Red stain indicates presence of calcium on the scaffold surface and the inserts at 21 days show the calcium deposits [Bar= 0.5mm].

4 Conclusions

In this study 3D printed composite scaffolds based on PCL, PCL/HA and PCL/SrHA were fabricated by advantageous extrusion-based 3D printing technology. MicroCT analysis revealed a reliable approach in providing information on the total porosity values (which resulted in the range of human cancellous bone) of the different architectures produced, also showing that all the printed scaffolds displayed a high level of fidelity to the original CAD model. In terms of biomechanical performance, the presence of the ceramic phase (up to 20 wt%) in the polymeric matrix led to not statistically significant differences in the values of Young's moduli in comparison to bare PCL scaffolds. Thus, it can be stated that the material formulation broadly unaffected the mechanical properties of the manufactured 3D scaffolds, which to some extent can be tailored through the adjustment of the scaffold architecture. Moreover, concerning the biological performance, both polymeric and composite 3D printed scaffolds showed good levels of biocompatibility and a favourable support for cells' attachment, growth and proliferation. However, the SrHA containing scaffolds exhibited higher levels of mineralisation with respect to bare PCL and PCL/HA scaffolds following *in vitro* assays, hence indicating their promise for bone tissue engineering applications.

Acknowledgment

This work was financially supported by Ulster University (Research Challenge Fund, 2018 competition) and The North West Centre for Advanced Manufacturing (NW CAM) project, a European Union's INTERREG VA Programme, managed by the Special EU Programmes Body (SEUPB). The views and opinions in this document do not necessarily reflect those of the European Commission or the Special EU Programmes Body (SEUPB). If you would like further information about NW CAM please contact the lead partner, Catalyst, for details.

References

[1] Baroli B. From natural bone grafts to tissue engineering therapeutics: brainstorming on pharmaceutical formulative requirements and challenges. Journal of pharmaceutical sciences. 2009;98(4):1317-1375.
[2] Liu D, Nie W, Li D, Wang W, Zheng L, Zhang J, et al. 3D printed PCL/SrHA scaffold for enhanced bone regeneration. Chemical Engineering Journal. 2019;362:269-279.
[3] Goncalves EM, Oliveira FJ, Silva RF, Neto MA, Fernandes MH, Amaral M, et al. Three-dimensional printed PCL-hydroxyapatite scaffolds filled with CNT s for bone cell growth stimulation. Journal of Biomedical Materials Research Part B: Applied Biomaterials. 2016;104(6):1210-1219.
[4] Liu T, Huang K, Li L, Gu Z, Liu X, Peng X, et al. High performance high-density polyethylene/hydroxyapatite nanocomposites for load-bearing bone substitute: fabrication, in vitro and in vivo biocompatibility evaluation. Composites Science and Technology. 2019;175:100-110.
[5] Campana V, Milano G, Pagano E, Barba M, Cicione C, Salonna G, et al. Bone substitutes in orthopaedic surgery: from basic science to clinical practice. Journal of Materials Science: Materials in Medicine. 2014;25(10):2445-2461.
[6] Wang W, Yeung KW. Bone grafts and biomaterials substitutes for bone defect repair: A review. Bioactive materials. 2017;2(4):224-247.
[7] Fernandez de Grado G, Keller L, Idoux-Gillet Y, Wagner Q, Musset A-M, Benkirane-Jessel N, et al. Bone substitutes: a review of their characteristics, clinical use, and perspectives for large bone defects management. Journal of tissue engineering. 2018;9:2041731418776819.
[8] Palazzo C, Ravaud J-F, Papelard A, Ravaud P, Poiraudeau S. The burden of musculoskeletal conditions. PloS one. 2014;9(3):e90633.
[9] Burg KJ, Porter S, Kellam JF. Biomaterial developments for bone tissue engineering. Biomaterials. 2000;21(23):2347-2359.
[10] Chocholata P, Kulda V, Babuska V. Fabrication of scaffolds for bone-tissue regeneration. Materials. 2019;12(4):568.
[11] Amini AR, Laurencin CT, Nukavarapu SP. Bone tissue engineering: recent advances and challenges. Critical Reviews™ in Biomedical Engineering. 2012;40(5).
[12] O'brien FJ. Biomaterials & scaffolds for tissue engineering. Materials today. 2011;14(3):88-95.
[13] Touri M, Kabirian F, Saadati M, Ramakrishna S, Mozafari M. Additive manufacturing of biomaterials− the evolution of rapid prototyping. Advanced Engineering Materials. 2019;21(2):1800511.
[14] Thavornyutikarn B, Chantarapanich N, Sitthiseripratip K, Thouas GA, Chen Q. Bone tissue engineering scaffolding: computer-aided scaffolding techniques. Progress in biomaterials. 2014;3(2-4):61-102.
[15] Rider P, Kačarević ŽP, Alkildani S, Retnasingh S, Schnettler R, Barbeck M. Additive manufacturing for guided bone regeneration: A perspective for alveolar ridge augmentation. International journal of molecular sciences. 2018;19(11):3308.
[16] Mellor LF, Huebner P, Cai S, Mohiti-Asli M, Taylor MA, Spang J, et al. Fabrication and evaluation of electrospun, 3D-bioplotted, and combination of electrospun/3D-bioplotted scaffolds for tissue engineering applications. BioMed research international. 2017;2017.

[17] Gregor A, Filová E, Novák M, Kronek J, Chlup H, Buzgo M, et al. Designing of PLA scaffolds for bone tissue replacement fabricated by ordinary commercial 3D printer. Journal of biological engineering. 2017;11(1):31.
[18] Shim J-H, Kim SE, Park JY, Kundu J, Kim SW, Kang SS, et al. Three-dimensional printing of rhBMP-2-loaded scaffolds with long-term delivery for enhanced bone regeneration in a rabbit diaphyseal defect. Tissue Engineering Part A. 2014;20(13-14):1980-1992.
[19] Song R, Murphy M, Li C, Ting K, Soo C, Zheng Z. Current development of biodegradable polymeric materials for biomedical applications. Drug design, development and therapy. 2018;12:3117.
[20] Kyle S, Jessop ZM, Al-Sabah A, Whitaker IS. 'Printability'of Candidate Biomaterials for Extrusion Based 3D Printing: State-of-the-Art. Advanced healthcare materials. 2017;6(16):1700264.
[21] Seidenstuecker M, Kerr L, Bernstein A, Mayr HO, Suedkamp NP, Gadow R, et al. 3D powder printed bioglass and β-tricalcium phosphate bone scaffolds. Materials. 2018;11(1):13.
[22] Ma Y, Dai H, Huang X, Long Y. 3D printing of bioglass-reinforced β-TCP porous bioceramic scaffolds. Journal of Materials Science. 2019;54(14):10437-10446.
[23] Cox SC, Thornby JA, Gibbons GJ, Williams MA, Mallick KK. 3D printing of porous hydroxyapatite scaffolds intended for use in bone tissue engineering applications. Materials Science and Engineering: C. 2015;47:237-247.
[24] Woodard JR, Hilldore AJ, Lan SK, Park C, Morgan AW, Eurell JAC, et al. The mechanical properties and osteoconductivity of hydroxyapatite bone scaffolds with multi-scale porosity. Biomaterials. 2007;28(1):45-54.
[25] Hoppe A, Güldal NS, Boccaccini AR. A review of the biological response to ionic dissolution products from bioactive glasses and glass-ceramics. Biomaterials. 2011;32(11):2757-2774.
[26] Mancuso E, Bretcanu OA, Marshall M, Birch MA, McCaskie AW, Dalgarno KW. Novel bioglasses for bone tissue repair and regeneration: Effect of glass design on sintering ability, ion release and biocompatibility. Materials & design. 2017;129:239-248.
[27] Murphy S, Boyd D, Moane S, Bennett M. The effect of composition on ion release from Ca–Sr–Na–Zn–Si glass bone grafts. Journal of Materials Science: Materials in Medicine. 2009;20(11):2207.
[28] Jha P, Singh K. Effect of MgO on bioactivity, hardness, structural and optical properties of SiO2–K2O–CaO–MgO glasses. Ceramics International. 2016;42(1):436-444.
[29] Abou Neel EA, Chrzanowski W, Pickup DM, O'Dell LA, Mordan NJ, Newport RJ, et al. Structure and properties of strontium-doped phosphate-based glasses. Journal of the Royal Society Interface. 2008;6(34):435-446.
[30] Ge M, Ge K, Gao F, Yan W, Liu H, Xue L, et al. Biomimetic mineralized strontium-doped hydroxyapatite on porous poly (l-lactic acid) scaffolds for bone defect repair. International journal of nanomedicine. 2018;13:1707.
[31] Florencio-Silva R, Sasso GRdS, Sasso-Cerri E, Simões MJ, Cerri PS. Biology of bone tissue: structure, function, and factors that influence bone cells. BioMed research international. 2015;2015.
[32] Zhang J, Xu S, Wang K, Yu S. Effects of the rare earth ions on bone resorbing function of rabbit mature osteoclastsin vitro. Chinese Science Bulletin. 2003;48(20):2170-2175.

[33] Ni GX, Shu B, Huang G, Lu WW, Pan HB. The effect of strontium incorporation into hydroxyapatites on their physical and biological properties. Journal of Biomedical Materials Research Part B: Applied Biomaterials. 2012;100(2):562-568.
[34] Capuccini C, Torricelli P, Sima F, Boanini E, Ristoscu C, Bracci B, et al. Strontium-substituted hydroxyapatite coatings synthesized by pulsed-laser deposition: in vitro osteoblast and osteoclast response. Acta Biomaterialia. 2008;4(6):1885-1893.
[35] Jammalamadaka U, Tappa K. Recent advances in biomaterials for 3D printing and tissue engineering. Journal of functional biomaterials. 2018;9(1):22.
[36] Zhang L, Yang G, Johnson BN, Jia X. Three-dimensional (3D) printed scaffold and material selection for bone repair. Acta biomaterialia. 2018.
[37] Choi D, Marra KG, Kumta PN. Chemical synthesis of hydroxyapatite/poly (ε-caprolactone) composites. Materials Research Bulletin. 2004;39(3):417-432.
[38] Chen G, Chen N, Wang Q. Fabrication and properties of poly (vinyl alcohol)/β-tricalcium phosphate composite scaffolds via fused deposition modeling for bone tissue engineering. Composites Science and Technology. 2019;172:17-28.
[39] Xiao X, Chevali VS, Song P, He D, Wang H. Polylactide/hemp hurd biocomposites as sustainable 3D printing feedstock. Composites Science and Technology. 2019;184:107887.
[40] Bittner SM, Smith BT, Diaz-Gomez L, Hudgins CD, Melchiorri AJ, Scott DW, et al. Fabrication and mechanical characterization of 3D printed vertical uniform and gradient scaffolds for bone and osteochondral tissue engineering. Acta biomaterialia. 2019;90:37-48.
[41] Melo P, Ferreira A-M, Waldron K, Swift T, Gentile P, Magallanes M, et al. Osteoinduction of 3D printed particulate and short-fibre reinforced composites produced using PLLA and apatite-wollastonite. Composites Science and Technology. 2019;184:107834.
[42] Cho YS, Quan M, Lee S-H, Hong MW, Kim YY, Cho Y-S. Assessment of osteogenesis for 3D-printed polycaprolactone/hydroxyapatite composite scaffold with enhanced exposure of hydroxyapatite using rat calvarial defect model. Composites Science and Technology. 2019;184:107844.
[43] Robinson L, Salma-Ancane K, Stipniece L, Meenan B, Boyd A. The deposition of strontium and zinc Co-substituted hydroxyapatite coatings. Journal of Materials Science: Materials in Medicine. 2017;28(3):51.
[44] Jebahi S, Oudadesse H, El Feki H, Rebai T, Keskes H, Pellen P, et al. Antioxidative/oxidative effects of strontium-doped bioactive glass as bone graft. In vivo assays in ovariectomised rats. Journal of Applied Biomedicine. 2012;10(4):195-209.
[45] Jebahi S, Oudadesse H, Elleuch J, Tounsi S, Keskes H, Rebai T, et al. The potential restorative effects of strontium-doped bioactive glass on bone microarchitecture after estrogen-deficieny induced osteoporosis: physicochemical and histomorphometric analyses. Journal of the Korean Society for Applied Biological Chemistry. 2013;56(5):533-540.
[46] Kim MH, Yun C, Chalisserry EP, Lee YW, Kang HW, Park S-H, et al. Quantitative analysis of the role of nanohydroxyapatite (nHA) on 3D-printed PCL/nHA composite scaffolds. Materials Letters. 2018;220:112-115.
[47] Yilgor P, Sousa RA, Reis RL, Hasirci N, Hasirci V. 3D plotted PCL scaffolds for stem cell based bone tissue engineering. Macromolecular symposia, vol. 269: Wiley Online Library; 2008. p. 92-99.

[48] Sobral JM, Caridade SG, Sousa RA, Mano JF, Reis RL. Three-dimensional plotted scaffolds with controlled pore size gradients: effect of scaffold geometry on mechanical performance and cell seeding efficiency. Acta biomaterialia. 2011;7(3):1009-1018.
[49] Cao X, Song P, Qiao Y, Zhen P. 3D printing of bone tissue engineering scaffolds. Chinese Journal of Tissue Engineering Research. 2015(25):4076-4080.
[50] Singh M, Dormer N, Salash JR, Christian JM, Moore DS, Berkland C, et al. Three-dimensional macroscopic scaffolds with a gradient in stiffness for functional regeneration of interfacial tissues. Journal of biomedical materials research Part A. 2010;94(3):870-876.
[51] Di Luca A, Ostrowska B, Lorenzo-Moldero I, Lepedda A, Swieszkowski W, Van Blitterswijk C, et al. Gradients in pore size enhance the osteogenic differentiation of human mesenchymal stromal cells in three-dimensional scaffolds. Scientific reports. 2016;6(1):1-13.
[52] Diaz-Gomez L, Smith BT, Kontoyiannis PD, Bittner SM, Melchiorri AJ, Mikos AG. Multimaterial segmented fiber printing for gradient tissue engineering. Tissue Engineering Part C: Methods. 2019;25(1):12-24.
[53] Moroni L, De Wijn J, Van Blitterswijk C. 3D fiber-deposited scaffolds for tissue engineering: influence of pores geometry and architecture on dynamic mechanical properties. Biomaterials. 2006;27(7):974-985.
[54] Londoño-Restrepo SM, Jeronimo-Cruz R, Millán-Malo BM, Rivera-Muñoz EM, Rodriguez-García ME. Effect of the Nano Crystal Size on the X-ray Diffraction Patterns of Biogenic Hydroxyapatite from Human, Bovine, and Porcine Bones. Scientific reports. 2019;9(1):5915.
[55] Neufurth M, Wang X, Wang S, Steffen R, Ackermann M, Haep ND, et al. 3D printing of hybrid biomaterials for bone tissue engineering: Calcium-polyphosphate microparticles encapsulated by polycaprolactone. Acta biomaterialia. 2017;64:377-388.
[56] Hassanajili S, Karami-Pour A, Oryan A, Talaei-Khozani T. Preparation and characterization of PLA/PCL/HA composite scaffolds using indirect 3D printing for bone tissue engineering. Materials Science and Engineering: C. 2019;104:109960.
[57] Prakash K, Ooi C, Kumar R, Khor K, Cheang P. Effect of super saturation level on the size and morphology of hydroxyapatite precipitate. 2006 IEEE Conference on Emerging Technologies-Nanoelectronics: IEEE; 2006. p. 345-349.
[58] Huang B, Caetano G, Vyas C, Blaker JJ, Diver C, Bártolo P. Polymer-ceramic composite scaffolds: The effect of hydroxyapatite and β-tri-calcium phosphate. Materials. 2018;11(1):129.
[59] Ghassemi T, Shahroodi A, Ebrahimzadeh MH, Mousavian A, Movaffagh J, Moradi A. Current concepts in scaffolding for bone tissue engineering. Archives of Bone and Joint Surgery. 2018;6(2):90.
[60] Jiang W, Shi J, Li W, Sun K. Morphology, wettability, and mechanical properties of polycaprolactone/hydroxyapatite composite scaffolds with interconnected pore structures fabricated by a mini-deposition system. Polymer Engineering & Science. 2012;52(11):2396-2402.
[61] Kim J-W, Shin K-H, Koh Y-H, Hah MJ, Moon J, Kim H-E. Production of poly (ε-caprolactone)/hydroxyapatite composite scaffolds with a tailored macro/micro-porous structure, high mechanical properties, and excellent bioactivity. Materials. 2017;10(10):1123.
[62] Gómez-Lizárraga K, Flores-Morales C, Del Prado-Audelo M, Álvarez-Pérez M, Piña-Barba M, Escobedo C. Polycaprolactone-and polycaprolactone/ceramic-based 3D-bioplotted porous scaffolds for bone regeneration: A comparative study. Materials Science and Engineering: C. 2017;79:326-335.

[63] Melo P, Tarrant E, Swift T, Townshend A, German M, Ferreira AM, et al. Short phosphate glass fiber-PLLA composite to promote bone mineralization. Materials Science and Engineering: C. 2019;104:109929.